International Shipbuilding Progress 60 (2013) 277–308
DOI 10.3233/ISP-130098
IOS Press

Simulation based design optimization of waterjet propelled Delft catamaran

Manivannan Kandasamy [a], Daniele Peri [b], Yusuke Tahara [c], Wesley Wilson [d], Massimo Miozzi [b], Svetlozar Georgiev [e], Evgeni Milanov [e], Emilio F. Campana [b] and Frederick Stern [a,*]

[a] *IIHR, Hydroscience and Engineering, University of Iowa, Iowa City, USA*
[b] *INSEAN-CNR, National Research Council, Maritime Research Centre, Rome, Italy*
[c] *NMRI, National Maritime Research Institute, Tokyo, Japan*
[d] *NSWCCD, Naval Surface Warfare Center Carderock Division, Bethesda, MD, USA*
[e] *BSHC, Bulgarian Ship Hydrodynamics Center, Varna, Bulgaria*

The present work focuses on the application of simulation-based design for the resistance optimization of waterjet propelled Delft catamaran, using integrated computational and experimental fluid dynamics. A variable physics/variable fidelity approach was implemented wherein the objective function was evaluated using both low fidelity potential flow solvers with a simplified *CFD* waterjet model and high fidelity *RANS* solvers with discretized duct flow calculations. Both solvers were verified and validated with data for the original hull. The particle swarm optimizer was used for single speed optimization at Fr $=$ 0.5, and genetic algorithms were used for multi speed optimization at Fr $=$ 0.3, 0.5 and 0.7. The variable physics/variable fidelity approach was compared with high fidelity approach for the bare-hull shape optimization and it showed an overall *CPU* time reduction of 54% and converged to the same optimal design at Fr $=$ 0.5. The multi-speed optimization showed design improvement at Fr $=$ 0.5 and 0.7, but not at Fr $=$ 0.3 since the design variables were obtained based on sensitivity analysis at Fr $=$ 0.5. High fidelity simulation results for the optimized barehull geometry indicated 4% reduction in resistance and the optimized waterjet equipped geometry indicated 11% reduction in effective pump power required at self-propulsion. Verification was performed for the optimized hull form and its reduction in powering will be validated in forthcoming experimental campaign.

Keywords: Simulation-based design, ship design, waterjet propulsion, variable fidelity

1. Introduction

Waterjet (*WJ*) propulsion features shallow draft design, smooth engine load, less vibration, lower water borne noise, no appendage drag, better efficiency at high speeds and good maneuverability. Pre-designed waterjets are readily available for any type of vessel based on the engine power, resistance curves, and the design speed of the ship. However, the performance of the *WJ* systems with respect to inlet efficiency, velocity distribution at the impeller plane, and cavitation inception at

*Corresponding author. E-mail: Frederick-stern@uiowa.edu.

cutwater, rely on the inlet velocity ratio (*IVR*), which depends on the specific hull shape in addition to the speed of operation. Optimization of the pre-designed waterjets with regard to the specific hull forms would considerably improve the powering performance.

Recent developments in *CFD* and high performance computing have significantly advanced simulation-based design (*SBD*) optimization of ship hull forms and greatly reduced the cost incurred by traditional build and test approaches. Campana et al. [5] provides an overview of all the relevant aspects involved in the development of an up-to-date *SBD* framework for ship design: optimization algorithms to explore the design space in search for the optimum design, automatic mesh and geometry modifiers and analysis tools for evaluating the objective function and drive the optimization algorithm.

The analysis tools used for *SBD* optimization vary in levels of approximation, progressing from linear 2D slender body theory, to non-linear 3D panel methods, to detailed *RANS* calculations including all ship appendages. Stern et al. [26] gives a detailed overview of the different fidelity codes used at different stages of the *SBD* process. Combinations of different methods, namely "zonal" or "domain decomposition" approaches have also been developed. Janson and Larson [14] divided the domain into three zones for the simulation-based optimization of a series 60 hull. The first zone covers the entire hull and a part of its surrounding free-surface and uses a free-surface Rankine-source type potential-flow method. The second zone is a thin layer at the hull surface and uses a momentum integral type boundary layer method. The third zone includes the aft part of the hull and uses *RANS*. The zones are computed in sequence and boundary conditions are generated for succeeding zones. This approach reduces the computational time considerable compared to a full *RANS* solver. However, since the viscous non-linear effects on the waves were neglected, experiments carried out for the original and the optimized hull did not validate the resistance improvements obtained in the computations. The computations predicted the right trend, but underpredicted the wave resistance magnitude. Consequently, the authors recommend the use of a Navier–Stokes solver with free-surface calculations for future work. Similar observation was made by Kandasamy et al. [17] where the early stage potential flow optimization predicted the correct trend but underpredicted the wave resistance magnitude for a foil-assisted semi-planning catamaran.

Numerical optimization algorithms for automatic optimal design are independent of the flow-solver complexity, which is however an issue (and has to be properly treated via variable fidelity and/or metamodels approaches, see Campana et al. [5]) when the computational cost is large. Gradient based optimization methods are classified as local optimization schemes since they require the calculation of the gradient of the objective function and hence may get stuck in a local minimum. Meta-heuristic optimization methods such as genetic algorithms and particle swarm optimizers are classified as global optimization algorithms since they are derivative-free and less prone to getting stuck in a local minimum. However, they are much more expensive in terms of number of objective function evaluations needed for the achievement of

the convergence of the algorithm, and they are typically very slow to converge at the precise optimal value. Finally, the way in which the automatic geometrical and volume (or surface) grid changes are handled is the third important block of any *SBD* tool. The computational grid adopted in the analysis must be deformed, in background, each time there is a new perturbed design to be evaluated, trying to preserve at the same time the quality of the new mesh. In conjunction with *RANS* solvers, regridding issues may become extremely relevant to the performance and the final result of the optimization.

The main objective of the current hydrodynamic optimization was to implement a multi-pronged parallel optimization for powering optimization of a *WJ*-propelled catamaran at Fr $= 0.5$, using different features of the *SBD* toolbox. A complementary multi-speed optimization study was also carried out for three different speeds, Fr $= 0.3$, 0.5 and 0.7. The toolbox used for the optimization is a product of the long-term ongoing collaboration between IIHR, INSEAN and NMRI research groups. The toolbox consists of the high fidelity (HF) *URANS* solver CFDShip [6], and the low fidelity (LF) linearized potential flow solver WARP [2], two evolutionary optimization algorithms, namely a multi-objective genetic algorithms – MOGA [29] and a particle swarm optimization (PSO) method [5]. It also contains different geometry modification tools and meta-modeling techniques, namely a free form deformation (FFD) approach [4] and different morphing techniques. Previous versions of the toolbox have been successfully used for progressively complex designs, namely, mono-hull surface combatant [4], multi-hull high speed sea lifts [29], *SWATH* displacement ships [28], foil-assisted semi-planing catamaran ferries [17] and uncoupled barehull and *WJ* inlet optimization of JHSS mono-hull [18]. The current study extends the *SBD* toolbox to the water-jet propelled Delft catamaran (*DC*) that has pronounced *WJ*-hull interaction caused by the hull contour at inlet, unlike JHSS that has a flat intake. The absence of gooseneck and multiple adjacent waterjets makes it more cost-effective for forthcoming build and test validation of the optimized hull form. The multi-hull geometry provides additional opportunities to explore asymmetric effects of the demi-hulls on wave interference and inlet air-entrainment. Sufficient model testing data of the original hull is available for code validation and data has already been used as a benchmark for many hydrodynamic performance and validation studies; e.g., effects of separation distances [12], sea-keeping [7], manoeuvring [19], and also for the development of the integral force/moment *CFD WJ* model [16].

Since viscous effects involving boundary layer ingestion play a significant part in the *WJ*-hull interaction efficiency and the *WJ* inlet ducting efficiency, potential flow methods cannot be used for the duct inlet optimization. Hence, a variable physics approach is used for initial hull-form optimization with the simplified *CFD WJ* model to replicate the effects of the *WJ* without simulating the duct flow. The best performing hull is then attached with the discretized *WJ* duct for detailed inlet optimization using the high fidelity *RANS* solver with an actuator disk model to replicate the effects of the impeller.

2. *SBD* methodology

The *SBD* methodology comprises of three main parts: the optimizer, the geometry modification methods and the analysis tools (in the case of fluid dynamic optimization the latter are flow solvers, Fig. 1). The analysis tools send the evaluated objective functions for a certain set of design variables to an optimizer, which searches for their minimum value under the general non-linear programming mathematical framework and continually updates the design variables. Geometry modeling methods provides the link between the two by deforming the hull shape based on the updated design variables.

2.1. Optimizers

The *SBD* toolkit features two derivative-free, global optimization algorithms: PSO is a single/multi-objective global optimization algorithm and MOGA that is primarily a multi-objective optimization algorithm, but can also be used for single objective problems by setting the second objective function equal to the first one. MOGA is a stochastic algorithm, since the final results depends on the random variables involved in the initial formulation, whereas a new deterministic version of the original stochastic.

2.2. Geometry modification methods

Three different options are available for parametric design: B-splines, FFD technique and morphing. With B-splines, the hull form deformation is controlled by the position, direction and magnitude of the knot vectors that form the basis of the design variables. With FFD, the hull form is embedded into a parallelepiped, split by a number of coordinate planes. Crossings between the planes are the control points of the FFD, and the movement of the control-points results in the deformation of the volume, and the embedded hull. With morphing [24], the grid points are obtained as the weighted sum of the corresponding corners of the base grids, and weights are represented by the design variables of the optimization problem.

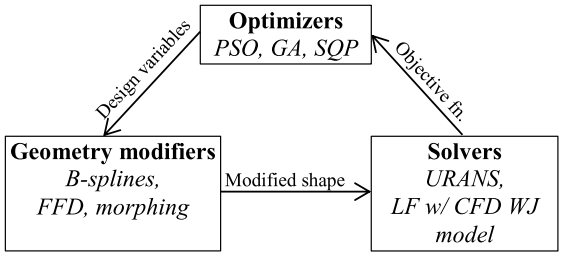

Fig. 1. *SBD* toolbox and methodology.

2.3. Solver methods

Two options are available for the choice of flow solver CFDShip-Iowa developed at IIHR is used as HF analysis tool, and the potential flow solver WARP, developed at INSEAN is adopted as LF code.

2.3.1. CFDShip-IOWA

The *URANS* solver uses a single-phase level set method to predict the free surface. A second order upwind scheme is used to discretize the convective terms of momentum equations and a pressure-implicit split-operator algorithm is used to enforce mass conservation on the collocated grids. The pressure Poisson equation is solved using the *PETSc* toolkit. All the other systems are solved using an alternating direction implicit method. For a high performance parallel computing, a MPI-based domain decomposition approach is used, where each decomposed block is mapped to one processor. A simplified body force model is used for *WJ* simulation to prescribe axisymmetric body force within the duct.

2.3.2. WARP

The WARP potential code is a classical boundary-element method solver. To solve numerically the set of integral equations arising from the Laplace equation arising from the potential flow description of the problem, the wetted hull surface and a region of the free surface are discretized into plane elements of quadrilateral shape. The free surface boundary conditions are linearized around the calm water level. Derivatives of the velocity potential are obtained analytically. The viscous terms are not directly considered during the solution, and an accurate estimate of the wave resistance is obtained, by pressure integration or by wave cut analysis. The frictional contribution is obtained by means of a locally adapted *ITTC* formula, where a local Reynolds number is used for each panel, based on the local velocity. The code allows for free sinkage and trim: the hull position is obtained by the equilibrium of the forces on the hull and the *WJ* induced forces and moments prescribed by the simplified *CFD WJ* model.

2.3.3. Water-jet models

The *WJ* duct flow can either be simulated through a discretized duct with an embedded actuator disk model to replace the pump system, or by using the simplified *CFD WJ* model to replace the whole duct control volume.

Simulations with embedded actuator disk model for *WJ* propelled JHSS have been validated recently by Delaney et al. [9] without free-surface calculations, and Takai et al. [31] who included free-surface calculations. Delaney et al. [9] indicated that the exclusion of the shaft in the actuator model had negligible influence on the performance analysis of the *WJ* system and they showed less than 1% error for self-propulsion flow rate, whereas Takai et al. [31] showed a 6% error which is attributed to overset grid interpolation errors within the duct.

The simplified *CFD WJ* model is used here to incorporate the effects of the *WJ* induced vertical forces and pitching moments on the sinkage and trim of the hull,

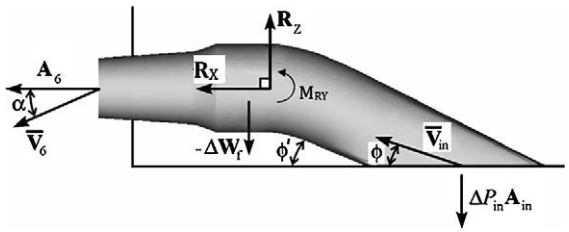

Fig. 2. *CFD* Waterjet model control volume.

without requiring detailed simulations for the *WJ* duct flow during the bare-hull optimization. The model uses the control volume shown in Fig. 2, which is selected with consideration to implementation simplicity in *CFD* using the same bare-hull grid by representing the *WJ* system by vertical reaction forces and pitching reaction moment, and by representing the *WJ*/hull interaction using a vertical stern force. The detailed duct flow calculations from the original hull provide the *WJ* induced vertical forces and pitching moments to be used during the hull shape optimization. Details of the model are provided in Kandasamy et al. [16] who validated its usage for *WJ* propelled DTMB-5594. Detailed waterjet flow simulation results from JHSS and *DC* were also used to investigate feasibility of deriving correlations based on the *WJ* geometry and *IVR* at working point. Ultimately, the model will be of most use if these generalized correlations can be obtained, which would provide the *WJ* induced forces and moments without prior experiments and/or detailed simulations of the duct flow.

2.4. Variable fidelity/variable physics approach

Numerical optimization in the naval field is shifting toward the use of High Fidelity (HF) *CFD* solvers, increasing the level of the physical content of the applied mathematical models adopted to guide the optimizer. This is done at the expense of computational power required for the analysis of the different designs, required during the course of the optimization.

One possible strategy to reduce the computational effort is to reduce the calls to the HF solver using approximation and/or interpolation models. A limited number of expensive HF simulations that sample the design space by some proper technique is used to obtain an approximation of the objective function (a meta-model, e.g. [23]). The optimization is then carried out using the meta-model whereas the optimum is checked using the HF code. The accuracy of the meta-model is then increased with every new point and the process is iterated until some kind of convergence is obtained.

The main criticism formulated for the use of meta-models is based on the difficulties in deriving a reliable approximation of the objective function when the number of variables is not small. An attractive alternative is based on the idea of exploiting two

or more physical models of different complexity (fidelity) for computing the same objective function. A Low Fidelity (LF) solver, fast but relatively simple, is adopted in conjunction with a High Fidelity (HF) solver, more reliable but time consuming. This simple – and old idea in engineering approaches to solve complex problems – is then "reinforced" with a solid mathematical background for the determination of the *correlation law* between HF and LF that gives an answer to the obvious question of *when* to switch from HF to LF and vice-versa. This represent the core of the *VF/VP* approach. The problem is solved using the fast LF tool, and the *trust region* approach (the mathematical theory) gives the rules for the systematic switch from LF to HF. Large *CPU* time savings (of the order of 50% and more, depending of the application) are obtained while the consistency between the two formulations (with and without *VF/VP*) is guaranteed.

The first proposal of the formulation of the *VF/VP* framework was presented for gradient based approaches and local optimization problems [1]. The essence of the idea stems from the basic Taylor series: any continuous and differentiable function of N variables can be locally expanded in Taylor series, so that in the neighborhood of the computational point x^0 holds the relationship:

$$f(x) = f\left(x^0\right) + \sum_{i=1}^{N} \frac{\partial f}{\partial x_i}\left(x_i - x_i^0\right) + \mathcal{O}^2. \tag{1}$$

Now, if we have two different models (LF and HF) to compute the same objective function, we can define a gap function as the difference of the two values at any x point of the *N*-design space:

$$\beta(x) = f^{\mathrm{HF}}(x) - f^{\mathrm{LF}}(x). \tag{2}$$

So that:

$$f^{\mathrm{HF}}(x) = \beta(x) + f^{\mathrm{LF}}(x). \tag{3}$$

From Eq. (3) follows that *if* the value of $\beta(x)$ is known over all the space, the HF would have been not needed anymore. The value of the *LF* function plus the gap function β would have then given the correct HF value. The problem is therefore shifted on the computation/evaluation of $\beta(x)$, in which the Taylor series intervenes. If we apply a Taylor expansion of β around the current design point x^0, and we stop at the first order as in previous equation, we obtain an approximation of β, say β^T. Obviously, β^T is exact only at the linearization point x^0, while some discrepancies arise once we move away from x^0. We call *trust region* the portion of space in which the β^T model is considered *trustable*, i.e. sufficiently accurate. This region is assumed spherical and centered in the linearization point x^0 and with *trust-region* radius ρ that can be adjusted dynamically.

The missing quantities to compute β^T are the value of $\beta(x^0)$ and the derivatives of $\beta(x)$ with respect to the design variables. If we are using a derivative-based optimization algorithm, these quantities are needed in any case, and we can compute them at the first step of the optimization algorithm. Since then, we are using the LF values plus correction, and we check the correctness of the approximation β^T by comparing the true HF value and the approximated $\text{HF}^T = \beta^T + \text{LF}$. In a derivative-based algorithm, two different phases are identified: firstly, the gradient of the function is computed, and it is applied as is, or combined with previous values, in order to detect a descent direction. After that, a line search is performed along the descent direction and the minimum value of the objective function is identified along this line. All the computations required in these phases are computed by using LF prediction plus β^T. At the end of the line search, HF is computed and compared with HF^T, and the relative difference is evaluated as

$$r = \frac{\text{HF}_2 - \text{HF}_1}{\text{HF}_2^T - \text{HF}_1^T}. \tag{4}$$

Where subscripts 1 and 2 indicate respectively the initial and final point of the line search: r represents the ratio between the real and estimated improvement. We can call it consistency check, since this is checking the consistency between the full HF problem and the *VF/VP* problem. If r is sufficiently close to the unit value, we can trust the local model β^T inside this region and the trust region radius can be increased. On the contrary, this is a sign that we cannot trust the model up to that distance, and the radius of the region is to be reduced: the step length of the line search is reduced, and another solution is computed, and the consistency check repeated. If the check fails repeatedly, and becomes too small, the model is recomputed and re-initialized.

This classical formulation is well suitable for local optimization methods based on derivatives. Results for ship design applications are reported in [23], where savings of about 75% are obtained. However, if a global optimization algorithm is applied, and derivatives are not computed, the framework is no longer convenient, since the initialization of the approximated model β^T requires the derivatives of both the LF and HF objective function. Consequently, a global approximation/interpolation model of the scaling factor β is needed: in this case, kriging interpolation model is applied. The trust region radius is no longer a singled value function, but depends on the computational point. Since we are using PSO algorithm for optimization, we can assign a different ρ^i for each (ith) particle of the swarm. Each time both HF and LF are computed, the consistency check is performed. If the new position of the particle is located inside the trust region, HF is not computed, and only LF plus correction is adopted. If the current best is improved, HF is computed, since the new position would replace one of the attractors of the swarm, and we must verify the accuracy of the prediction by $\beta^T + \text{LF}$.

3. Experimental methods

3.1. Model design and test plan

BSHC constructed a *DC* model with the main particulars tabulated in Table 1 and equipped it with available stock *WJ*.

Initial testing showed excessive swirl and immersion of the nozzle, which was rectified by adding extra fins at the stator and reducing the nozzle diameter. The new design showed significant reduction in swirl and nozzle immersion. The *DC* model was then shipped to INSEAN, who repeated the self-propulsion tests as a precursor to forthcoming validation tests on the optimized design.

For towed bare hull (BH) experiments, the difference between the two facilities was the location of the vertical pivot point. BSHC had a pivot point located above the $LCG = 1.91$ m with $KG = 0.28$ m, whereas INSEAN used hinges at FP and AP and adjustable height sliding towing post which allowed the pitch motions to be centered about the center of gravity during self-propulsion tests, i.e., $LCG = 1.91$ m, $KG = 0.34$ m.

For self-propelled (SP) experiments, BSHC assumed symmetry and performed measurements only on the starboard side *WJ*, whereas INSEAN performed measurements on both sides to account for installation uncertainty between the port and the starboard waterjets. Both facilities followed the ITTC [13] procedural guidelines described in detail in [20] and [21].

3.2. Overview of WJ test procedures

The ITTC Propulsion Committee [13] recommends the '*momentum flux method*' using control volume analysis for prediction of the powering performance of a *WJ*

Table 1
Particulars of the *DC* geometry

Main particulars	Symbol	Model
Length overall, m	L_{OA}	3.8220
Length between perpendiculars, m	L_{PP}	3.6274
Length on waterline, m	L_{WL}	3.6274
Breadth moulded, single hull, m	B	0.2904
Clearance b/n hull CPs, m	–	0.8470
Draft at FP, m	T_{F}	0.1815
Draft at AP, m	T_{A}	0.1815
Displacement volume, m^3	Δ	0.0770
Prismatic coefficient*	C_{P}	0.6160
Block coefficient*	C_{B}	0.4027
Longitudinal C.B.**	LCB	−0.0970
Wetted surface area (bare hull), m^2	5	1.4220

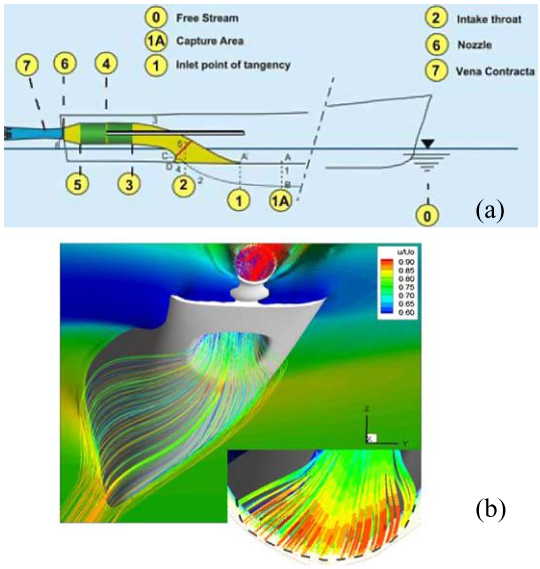

Fig. 3. Control volume for momentum-flux method: (a) EFD stations, (b) CFD inflow boundary shape. (Colors are visible in the online version of the article; http://dx.doi.org/10.3233/ISP-130098.)

driven ship [32]. The control volume shown in Fig. 3(a) is defined by a stream-tube consisting of the inlet (AB), an upstream imaginary surface in the flow through which it is assumed no mass transport occurs (BC), ducting system, pump, nozzle and outlet. The control volume boundaries capture all inflow, outflow of *WJ* system, and provide ease of measurement of volume flow-rate (Q_{SP}), and momentum and energy fluxes.

For all tested craft speeds, the inflow boundary was assumed rectangular and its size was determined from BH inlet velocity-field measurements. Fig. 3(b) shows the *CFD* inflow boundary at Fr $= 0.5$, which is elliptical similar to previous simulations [31]. Van Terwisga [32] concluded that the inlet capture area for Athena was also elliptical, but the shape does not have significant effect on the ingested momentum and energy flux. The net jet thrust (T_{NET}) of the *WJ* system is obtained from the net rate of change of momentum over the control volume.

The *WJ*-hull system is decomposed into a BH system and a *WJ* system. This facilitates independent evaluation of the pump efficiency (η_{pump}), ducting efficiency (η_{duct}), jet efficiency (η_{jet}), and the thrust deduction factor $(1-t)$ that constitute the overall *WJ* system efficiency (η_d). Note that the last term $(1-t)$ can be alternatively expressed as a product of wake fraction $(1-w)$, and hull efficiency $\eta_{\mathrm{H}} = (1-t)/(1-w)$, but were not essential for the present application, which focusses mainly on η_{duct}.

$$\eta_d = \eta_{\mathrm{pump}} \times \eta_{\mathrm{duct}} \times \eta_{\mathrm{jet}} \times (1-t). \tag{5}$$

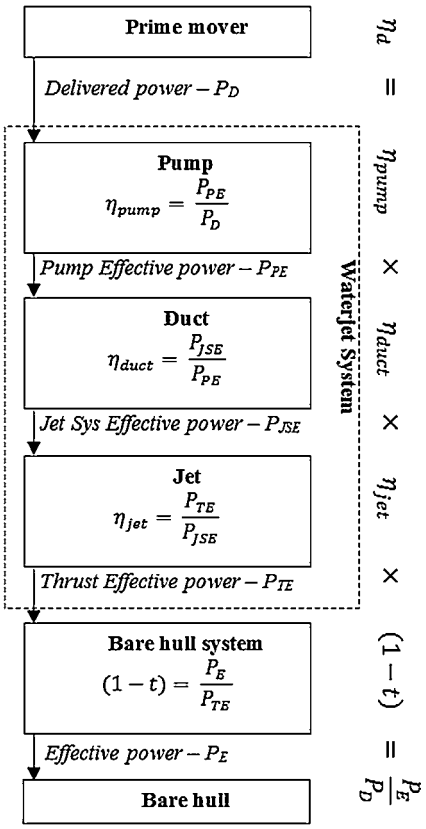

Fig. 4. Waterjet system decomposition.

Figure 4 illustrates the flow of energy from the prime mover to the BH system through the *WJ* system, which comprises of the pump, duct, and jet systems. The measured BH resistance (R_{BH}) and T_{NET} at SP velocity (V_{Ship}) allow for the calculation of P_{E} and P_{TE}, respectively.

$$P_{\text{E}} = R_{\text{BH}} \times V_{\text{Ship}}, \tag{6}$$

$$P_{\text{TE}} = T_{\text{NET}} \times V_{\text{Ship}}. \tag{7}$$

P_{JSE} is obtained from energy flux difference between station 7 ($E7$) and station 1 ($E1$), and P_{PE} is obtained from energy flux difference between station 5 ($E5$) and station 3 ($E3$).

$$P_{\text{JSE}} = E7 - E1, \tag{8}$$

$$P_{\text{PE}} = E5 - E3. \tag{9}$$

Table 2
Powering and motions U_{FB}

	BH			SP			
	R_{BH}	σ_{BH}	τ_{BH}	Q_{SP}	T_{NET}	σ_{SP}	τ_{SP}
U_{FB} (%$\bar{D}$)	0.7	7.7	9.8	0.1	0.7	2.9	0.9

P_{D} is obtained from the measured revolutions per second (n) and toque (τ)

$$P_{\mathrm{D}} = 2\pi \times n \times \tau. \tag{10}$$

The theoretical framework proposed by the specialist committee was standardized and validated by means of a rigorous experimental campaign from seven institutes on an Athena model at Fr $= 0.6$ [32]. Subsequently, NSWCCD conducted extensive *WJ* powering experiments the JHSS model equipped with four adjacent waterjets [15].

3.3. DC model test results

Quantitative estimation of facility bias [25] requires a minimum of three facilities. Here, data (D) is available from two facilities, and a qualitative estimate for facility bias (U_{FB}) can be obtained as a percent of the mean data ($\bar{D}$).

$$U_{\mathrm{FB}} = \left| \frac{D_{\mathrm{INSEAN}} - D_{\mathrm{BSHC}}}{2} \right| \%\bar{D}. \tag{11}$$

Figure 5 shows the data from the flow rate measurements of the bollard pull tests and the velocity profile measurements at stations 1 and 6, used for the momentum-flux analysis. Figure 6 compares $R_{\mathrm{BH}}, T_{\mathrm{NET}}, Q_{\mathrm{SP}}$, and the dynamometer shaft thrust (T_{S}) and Fig. 7 compares σ and τ for both BH (hollow symbols) and SP (filled symbols) conditions. For the towed BH tests, the facilities show very good agreement of all data up to Fr $= 0.5$. U_{FB} for R_{BH} progressively increases from 1.5% at Fr $=$ 0.5, to 3.5% at Fr $= 0.7$. U_{FB} for sinkage σ_{BH} increases with increasing Fr, and the resulting variation in dynamic wetted area accounts for larger U_{FB} for R_{BH} at higher Fr. Though the facilities have different vertical pivots, trim τ_{BH} shows good agreement over the entire Fr range with average $U_{\mathrm{FB}} = 9.8\%$. For Fr < 0.4, $\bar{D}$ for τ_{BH} approach zero resulting in large U_{FB} values.

For SP measurements, Q_{SP} shows very good agreement over the Fr range with average $U_{\mathrm{FB}} = 0.1\%$. Table 2 provides a summary of the U_{FB} values for the BH and SP measurements.

Figure 8 shows the comparison of the decomposed system efficiencies. Accurate calculation of P_{PE} requires measurement of pressure head at stations 3 and 5, which is challenging and expensive. Instead, both facilities used the product of T_{S} and V_{Ship} as an approximate measure for P_{PE}. Since energy fluxes at stations 1 and 7 were

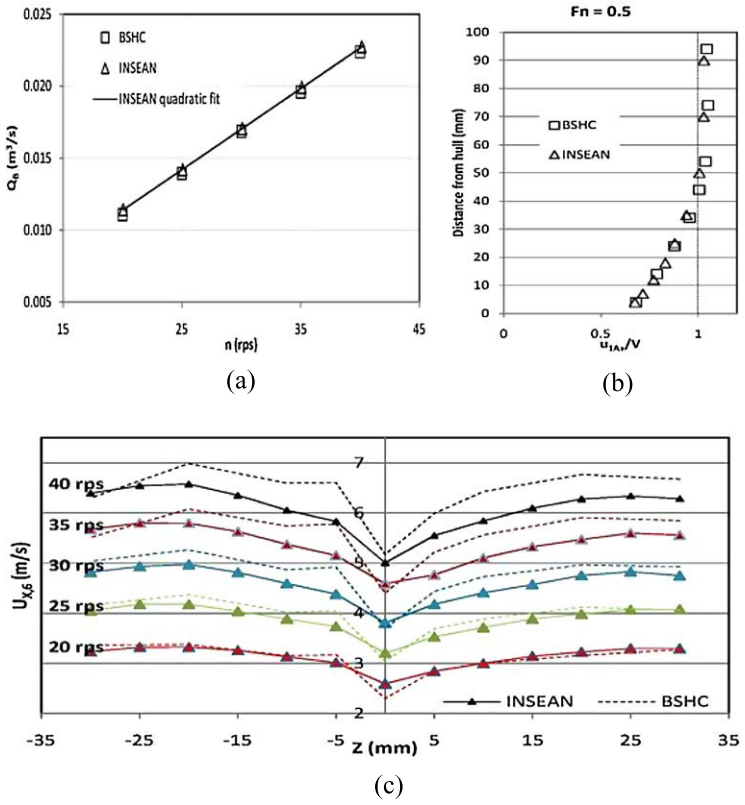

Fig. 5. Flow rate and velocity profiles: (a) Bollard pull flow rate measurements, (b) Velocity profile at station 1, (c) Velocity profile at station 6. (Colors are visible in the online version of the article; http://dx.doi.org/10.3233/ISP-130098.)

not calculated, P_{JSE} is unavailable and η_{duct} and η_{jet} are not decomposed. $\eta_{\text{duct}} \times \eta_{\text{jet}} = P_{\text{TE}}/P_{\text{PE}}$ is reported instead. U_{FB} values for the decomposed efficiencies are tabulated in Table 3.

3.4. Analysis of experimental results

3.4.1. Performance analysis of DC WJ

An indication of the *DC WJ* design performance is obtained by comparing its efficiencies with JHSS (Table 4) which serves as a benchmark [15]. All system efficiencies for *DC* are smaller than JHSS.

JHSS has a larger η_{pump} since the experiments used full-scale thrust loading similarity with the incorporation of an added tow force. The excess energy of the ingested working fluid due to the added tow force creates a higher ram pressure at the impeller

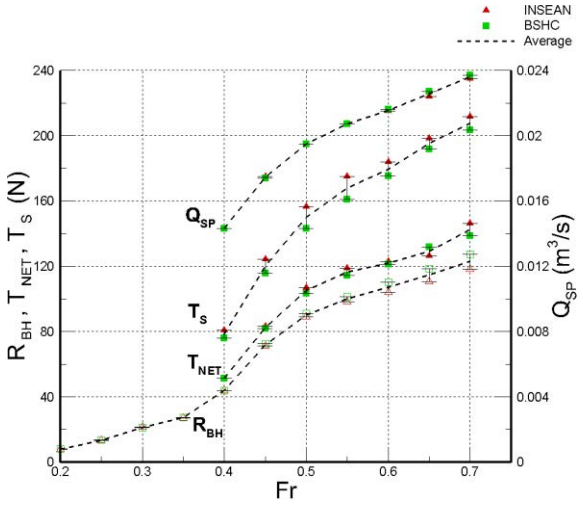

Fig. 6. Powering performance data. (Colors are visible in the online version of the article; http://dx.doi.org/10.3233/ISP-130098.)

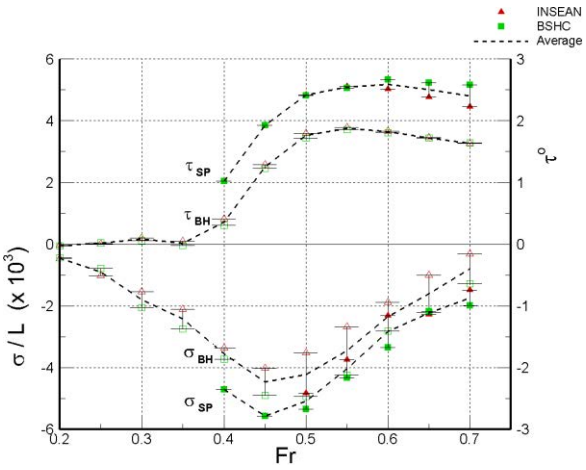

Fig. 7. Sinkage and trim data. (Colors are visible in the online version of the article; http://dx.doi.org/10.3233/ISP-130098.)

plane resulting in better pump performance. Without an added tow force, the *DC* requires larger Q_{SP} and n and the pump operates at a larger specific speed resulting in a reduced efficiency.

This disparity also accounts for the difference in thrust deduction factor $(1-t)$ as the larger Q_{SP} causes larger suction pressure at the inlet, and hence a greater increase in σ_{SP} and τ_{SP} resulting in larger T_{NET}.

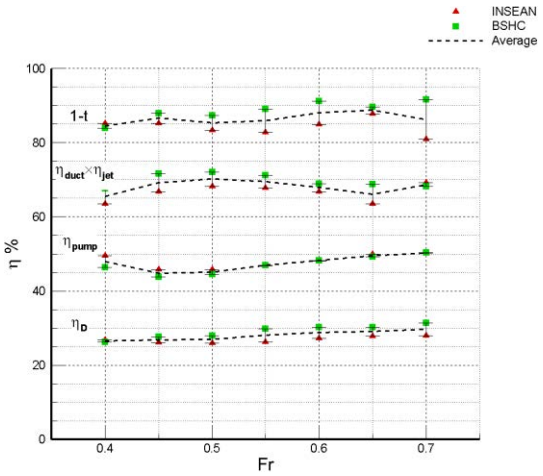

Fig. 8. Decomposed system efficiencies. (Colors are visible in the online version of the article; http://dx.doi.org/10.3233/ISP-130098.)

Table 3
Decomposed efficiencies U_{FB}

	η_D	η_{pump}	$\eta_{duct} \times \eta_{jet}$	$1-t$
U_{FB} (%$\bar{D}$)	2.1	0.5	1.3	1.2

Table 4
Decomposed efficiencies comparison

	η_D (%)	η_{pump} (%)	$\eta_{duct} \times \eta_{jet}$ (%)	$1-t$ (%)
DC	28	45	66	85
JHSS	45	58	85	91

The jet velocity ratio $JVR = V_{ship}/V_{jet}$ and $IVR = V_{ship}/V_{pump}$ influence η_{jet} and η_{duct} values, respectively. Note, to keep *JVR* and *IVR* values bounded when V_{ship} goes to zero, the definitions used here follow Bulten [3], which is the reciprocal of that used in some literature.

JVR for *DC* and JHSS are 0.60 and 0.66, respectively. For optimal η_{jet}, *JVR* values should be in the range of 0.65 and 0.75 [3]. Lower *JVR* values for *DC* result in excess axial kinetic energy loss into the wake, thereby reducing η_{jet}.

IVR for *DC* and JHSS are 1.83 and 1.7, respectively. Waterjets with *IVR* values greater than 1.8 have increased risk of separation at the top side of the inlet due to sudden flow deceleration [3], thereby reducing η_{duct}. *CFD* simulations confirmed the occurrence of flow separation for *DC*, making the inlet a good candidate for optimization.

Table 5
Comparison of U_{FB}

	T_{NET} (%)	Q_{SP} (%)	σ_{SP} (%)	τ_{SP} (%)
Athena	±18	±5	±116	±27
DC	±0.7	±0.1	±2.9	±0.9

3.4.2. Analysis of facility bias

The ITTC [13] standardized experimental campaign on the Athena model, which was conducted by seven facilities, provides a basis of comparison for U_{FB}. The values are compared in Table 5, and U_{FB} for *DC* are significantly smaller. Both BSHC and INSEAN participated in the experimental campaign on the Athena model, but have had limited experience with the *ITTC WJ* model since that time.

4. Verification and validation

Qualitative validations of the HF and LF solutions were performed for both BH and SP cases over the Fr range. Detailed quantitative verification and validation was performed for $\mathrm{Fr} = 0.5$.

4.1. Overview of V&V methodology

Verification and Validation procedures follow Stern et al. [27]. Verification procedures estimate numerical uncertainties (U_{SN}) based on iterative (U_{I}) and grid (U_{G}) uncertainties

$$U_{\mathrm{SN}} = \sqrt{U_{\mathrm{I}}^2 + U_{\mathrm{G}}^2}. \tag{12}$$

Grid convergence studies are carried out for three solutions (S) with systematic refinement ratio $r = \frac{\Delta x_2}{\Delta x_1} = \frac{\Delta x_3}{\Delta x_2}$, where 3, 2 and 1 represent the coarse, medium, and fine grids, respectively. Solution changes ε and the convergence ratio R are defined as $\varepsilon_{ij} = \mathrm{S}_i - \mathrm{S}_j$ and $R = \frac{\varepsilon_{12}}{\varepsilon_{23}}$. For monotonic convergence, $0 < R < 1$, factor of safety method [34] is used for estimations of U_{G}. The ratio $P = \frac{p_{\mathrm{RE}}}{p_{th}}$ is used to estimate the factor of safety and U_{G} is given by

$$U_{\mathrm{G}} = \begin{cases} (2.45 - 0.85P)|\delta_{\mathrm{RE}}|, & 0 < P \leqslant 1, \\ (16.4P - 14.8)|\delta_{\mathrm{RE}}|, & 1 < P, \end{cases} \tag{13}$$

where,

$$\delta_{\mathrm{RE}} = \frac{\varepsilon_{21}}{r^{p_{\mathrm{RE}}} - 1}. \tag{14}$$

For oscillatory convergence, $-1 < R < 0$, U_{G} is estimated from the upper and lower bounds of the oscillation. U_{G} is undefined for monotonic divergence, $R > 1$, and oscillatory divergence, $R < -1$.

Validation procedure defines the comparison error (E) and the validation uncertainty (U_{V}) using experimental benchmark data (D) and its uncertainty (U_{D}). If U_{V} bounds E, the combination of all the errors in D and S is smaller than U_{V} and validation is achieved at the U_{V} interval, where

$$\mathrm{E} = \mathrm{D} - \mathrm{S}, \tag{15}$$

$$U_{\mathrm{V}} = \sqrt{U_{\mathrm{D}}^2 + U_{\mathrm{SN}}^2}. \tag{16}$$

4.2. HF and LF models

Table 6 provides the *WJ* induced vertical forces (C_{Tz}) and moments (M_{Ty}) about the centre of gravity, non-dimensionalized by the V_{ship} and *LWL*.

Figure 9 shows the overset *WJ* grid used for HF simulations of duct flow using the actuator disk model. T_{net} and P_{PE} vary relative to the square and cube of Q_{SP}, respectively, and hence accurate prediction of Q_{SP} is vital. For the current study, the duct was discretized using a single structured grid, which overlaps with the hull grid

Table 6
WJ induced forces and moments

Fr	C_{Tz}	M_{Ty}
0.3	-0.03×10^{-4}	0.02×10^{-4}
0.5	-3.93×10^{-4}	1.61×10^{-4}
0.7	-1.35×10^{-4}	0.82×10^{-4}

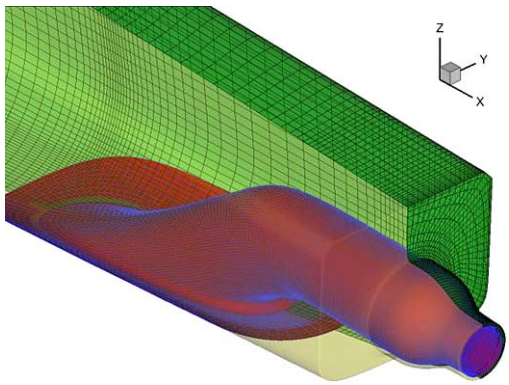

Fig. 9. Overset grid for duct discretization. (Colors are visible in the online version of the article; http://dx.doi.org/10.3233/ISP-130098.)

Table 7
Multi-block grid densities

Block #	Description	# grid pts
1	Inner-hull	3,540,908
2	Outer-hull	3,540,908
3	Duct	4,099,579
4	Refinement	2,285,061
5	Background	4,355,778
	Total	**17,822,233**

at the inlet and the nozzle exit since additional overset grids inside the duct cause interpolation errors as seen in Takai et al. [31].

Table 7 shows the fine grid (S_1) densities for the overset blocks used for the HF simulations. The HF and LF solvers used systematic refinement ratios $r = \sqrt{2}$ and 2, respectively.

For LF, the same number of grid panels has been used for hull and free surface: 6000 on S_1, 3000 on S_2 and 1500 on S_3, for a total number of panels of 12,000 on S_1, 6000 on S_2 and 3000 on S_3. For HF simulations the grids densities for S_1, S_2 and S_3 are 17.8M, 6.3M and 2.3M, respectively.

4.3. Qualitative validation over Fr *range*

HF solutions using the medium grid were obtained at Fr $= 0.3$, 0.5 and 0.7 for both BH and SP simulations. LF solutions were obtained over the Fr range for BH simulations, and at Fr $= 0.5$ using the simplified *CFD WJ* model. The solutions are compared with $\bar{D}$ over the Fr range in Fig. 10.

For BH simulations, R_{BH} for both HF and LF calculations agree well with $\bar{D}$. σ for LF calculations are under-predicted for Fr < 0.5 and over-predicted for Fr > 0.5 and τ calculations show a reversed trend. σ_{BH} for HF calculations are under-predicted for all values and τ_{BH} is under-predicted at Fr $= 0.5$.

For SP simulations, both HF and LF calculations under-predict T_{NET}, Q_{SP} and σ_{SP} for Fr $\geqslant 0.5$. Data is unavailable for Fr $= 0.3$. τ_{SP} is over-predicted by HF and under-predicted by LF.

4.4. Quantitative V&V at Fr $= 0.5$

At Fr $= 0.5$, a grid verification and validation study was conducted for both bare-hull and self-propelled simulations. R_{BH}, σ_{BH} and τ_{BH} for both LF and HF simulations are tabulated in Table 8. U_{I} is negligible and $U_{\text{SN}} = U_{\text{G}}$. Both HF and LF solutions show monotonic grid convergence for all the quantities. For all cases, $0 < R < 1$, and monotonic convergence was achieved. For HF calculations $P < 2$ and reasonably close to 1. For LF calculations $P > 3$, which make the U_{SN} calculations unreliable since the available database used by Xing and Stern [34] for the development of the factor of safety method was restricted to $P < 2$.

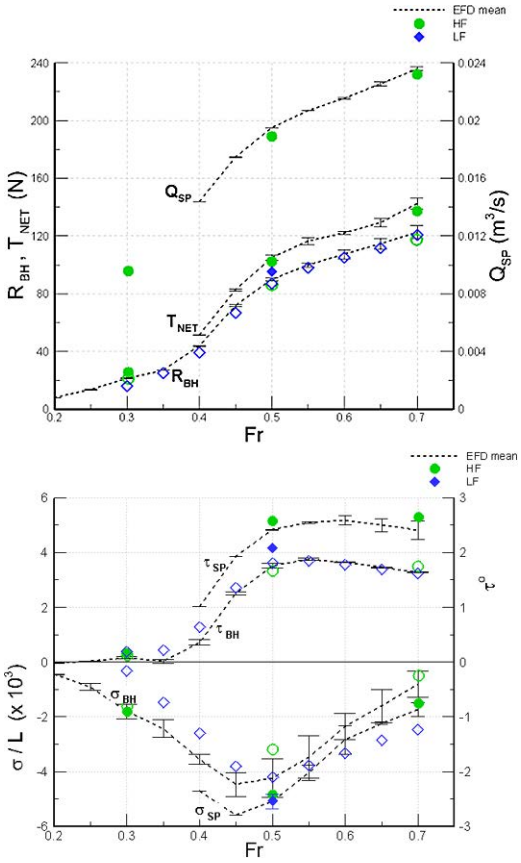

Fig. 10. Qualitative V&V. (Colors are visible in the online version of the article; http://dx.doi.org/10.3233/ISP-130098.)

Table 8
BH verification of HF and LF solutions

	S_3	S_2	S_1	R	P	U_{SN}
			HF BH			
R_{BH}	84.75	86.03	86.52	0.38	1.39	2.78
σ_{BH}	3.173	3.188	3.192	0.29	1.82	0.17
τ_{BH}	1.569	1.669	1.712	0.43	1.22	9.79
			LF BH			
R_{BH}	86.70	87.97	88.09	0.12	3.00	0.26
σ_{BH}	4.129	4.188	4.191	0.50	6.92	0.05
τ_{BH}	1.754	1.790	1.794	0.11	6.34	0.04

Table 9
BH validation of HF and LF solutions

	D	U_{FB}	U_{V}		E	
			HF	LF	HF	LF
R_{BH}	89.06	3.00	3.85	3.01	0.55	-1.09
σ_{BH}	3.182	1.31	1.31	1.31	0.20	31.57
τ_{BH}	1.751	1.00	9.84	1.00	2.33	2.63

Table 10
SP verification of *RANS* and LF solutions

	S_3	S_2	S_1	R	P	U_{SN}
			HF SP			
Q_{SP}	1.860	1.897	1.915	0.49	1.04	2.15
T_{NET}	96.16	102.02	104.22	0.38	1.41	2.91
σ_{SP}	4.731	4.855	4.762	–	–	1.29
τ_{SP}	2.763	2.585	2.687	–	–	3.64
P_{PE}	194.87	201.12	204.02	0.46	1.11	4.16
			LF SP			
T_{NET}	93.13	94.39	95.02	0.45	2.29	0.7
σ_{SP}	4.845	4.827	4.883	–	–	NA
τ_{SP}	2.081	2.123	2.140	0.49	2.08	2.14

Since precision and bias errors were not quantified in the experiments, U_{FB} was used for validation. D_{INSEAN} was used for calculating E, since the optimized hull will also be tested at that facility. Table 9 shows the results of the validation studies. Except for LF σ, whose |E| lies outside the U_{V} interval, all other solutions are validated.

For SP simulations, solutions HF calculations were verified and validated for Q_{SP}, T_{NET}, P_{PE}, σ_{SP} and τ_{SP}. P_{PE} was obtained by calculating energy difference between stations 5 and 3. LF calculations were verified and validated for T_{NET}, σ_{SP} and τ_{SP}. The HF and LF solutions are tabulated in Table 10. U_{I} is negligible and $U_{\text{SN}} = U_{\text{G}}$. HF solutions show monotonic grid convergence for Q_{SP}, T_{NET} and P_{PE}, and oscillatory convergence for σ_{SP} and τ_{SP}. LF solutions show monotonic grid convergence for T_{NET}, and τ_{SP}, and oscillatory divergence for σ_{SP}.

Table 11 shows the validation results for the different quantities. HF solutions |E| lie outside the U_{V} interval for P_{PE}. Note that the P_{PE} estimate from the experiments does not account for viscous energy losses between station 3 and 5, and hence is prone to over-estimation. LF solutions |E| lie outside the U_{V} interval for T_{NET}.

The numerical uncertainty levels are similar to than obtained for JHSS [31]. The validation errors are smaller than that for JHSS, due to the elimination of overset grids within the duct. For *DC*, $|\text{E}| = 2\%$ and 4% for Q_{SP}, and T_{NET}, respectively, compared to 5.6% and 6.5% for JHSS.

Table 11
SP validation of *RANS* and LF solutions

	D	U_{FB}	U_V		E	
			HF	LF	HF	LF
Q_{SP}	1.95	0.51	2.21	NA	−2.05	NA
T_{NET}	106.9	3.21	4.35	3.28	−4.17	−11.1
σ_{BH}	4.87	1.34	3.58	NA	−2.30	NA
τ_{BH}	1.75	2.91	2.47	3.61	−2.33	2.63
P_{PE}	232	8.20	9.22	NA	−12.06	NA

5. Single objective resistance optimization using *CFD WJ* model

To facilitate greater variability of the design space, IIHR, DTMB and INSEAN conducted initial geometry sensitivity studies with the *CFD WJ* model to determine a feasible design space using different approaches. Multiple geometries were obtained using different geometry modification techniques; B-spline, Free Form Deformation (FFD), and CREATE-SHAPE [33], with resistance reductions varying from 0.5% to 1.5% compared to the original geometry. A morphing method, which enables direct construction of the design space by integrating the best geometries from the different sensitivity studies, was used for the optimization. The overall optimization process used a four-pronged approach by IIHR, DTMB, NMRI and INSEAN:

- IIHR and DTMB performed a single objective PSO optimization for resistance at Fr $=$ 0.5 using different combinations of the initial geometries to explore different subset design spaces.
- INSEAN performed single objective PSO optimization for resistance at Fr $=$ 0.5 using both variable fidelity and high fidelity optimization using generalized FFD with PSO optimizer to investigate computational cost reduction.
- NMRI performed MOGA for resistance at three speeds: Fr $=$ 0.3, 0.5 and 0.7 [30].

The best BH geometries obtained for Fr $=$ 0.5 from the different optimization approaches were then verified using *RANS* with identical grid size, grid topology and solver convergence criteria. The best geometry (Fig. 11) showed a resistance reduction of 4% due to significant reduction of the interference region trough (Fig. 12) and was selected for subsequent *WJ* inlet optimization.

6. Design optimization for overall propulsive efficiency of *WJ* propelled hull

Figure 13 shows the results from the sensitivity analysis performed on the *WJ* inlet shape. The streamlines and C_P contours at the *WJ* inlet symmetry plane for the original geometry and the modified geometry are illustrated. Sensitivity analysis

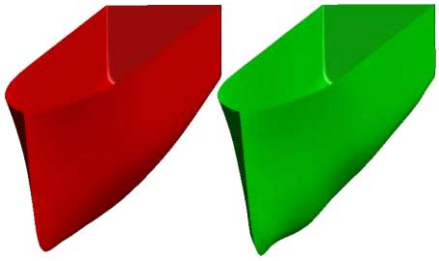

Fig. 11. Comparison of the original (red) and optimized (green) starboard demi-hulls. (The colors are visible in the online version of the article; http://dx.doi.org/10.3233/ISP-130098.)

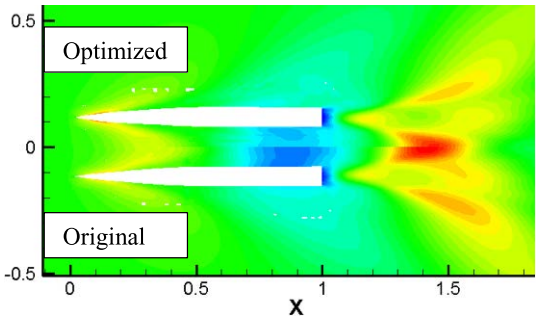

Fig. 12. Wave elevation comparison. (Colors are visible in the online version of the article; http://dx.doi.org/10.3233/ISP-130098.)

on the transition angle, inlet-angle and ramp-radius showed that a reduction of the angles, combined with an increase in the ramp radius with a widened inlet rectified the flow separation and increased η_{duct}.

Figure 14 illustrates the inlet ramp design variations intended for smoother transition and increasing boundary layer ingestion for recovery of residual kinetic energy lost to the wake.

The PSO optimization was performed on a coarse grid by morphing three initial geometries constructed with the three combinations of the design variables. The flow solver was tuned for trend identification with a liberal convergence criterion to increase computational speed. The optimal design indicated $\sim$10% reduction in P_{PE}. However, a grid refinement analysis of the optimized geometry revealed unforeseen problems: the fine grid solution predicted deeper trough at the stern with the free surface very close to the inlet, which was judged a possible cause of air ingestion into the *WJ* inlet. Therefore, local modifications on the inner side of the demi-hull – close to the *WJ*-inlet – were made (Fig. 15) and a geometrically constraint-based optimization was performed. The constraint was defined as the minimum distance function from the free surface to the inlet to be greater than or equal to the original Delft catamaran. Since the geometry variations were localized, the speed of the

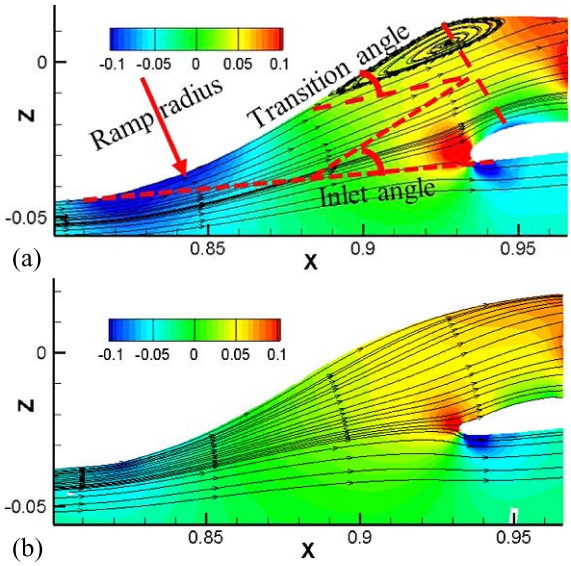

Fig. 13. Design variable sensitivity analysis: (a) original geometry, (b) modified geometry. (Colors are visible in the online version of the article; http://dx.doi.org/10.3233/ISP-130098.)

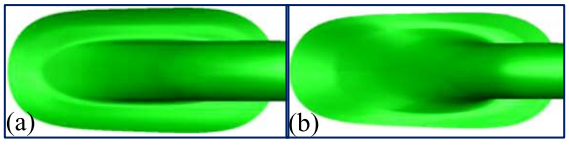

Fig. 14. Inlet ramp design variation: (a) original geometry, (b) modified geometry. (Colors are visible in the online version of the article; http://dx.doi.org/10.3233/ISP-130098.)

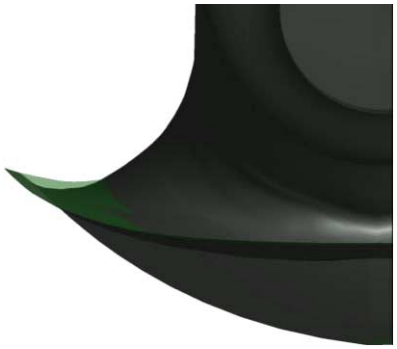

Fig. 15. Localized inlet design variations, green shade is the initial optimized geometry, grey shade is the modified design. (The colors are visible in the online version of the article; http://dx.doi.org/10.3233/ISP-130098.)

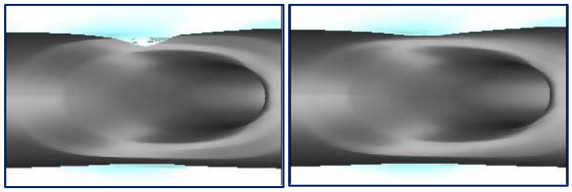

Fig. 16. Localized inlet design variations to minimize possibility of air entrainment. (Colors are visible in the online version of the article; http://dx.doi.org/10.3233/ISP-130098.)

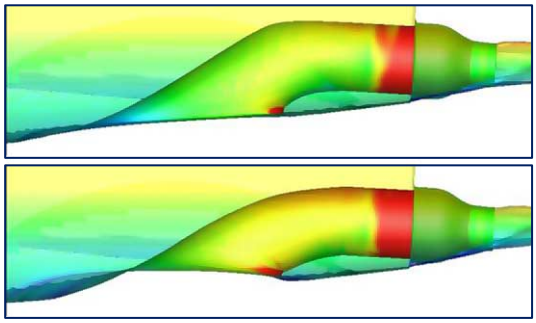

Fig. 17. Original and optimized waterjets. (Colors are visible in the online version of the article; http://dx.doi.org/10.3233/ISP-130098.)

fine grid computations was increased by using restart solution files from comparable geometries. The solutions for the final optimized geometry is shown in Fig. 16 compared to the initially optimized geometry.

Comparison of the duct surface pressure contours on the original and optimized hulls (Fig. 17) illustrates the increase in ram pressure on the forward facing walls of the optimized duct. This added potential energy develops additional pressure at the nozzle, which converts it to kinetic energy at exit and increases the *WJ* efficiency.

Detailed performance comparisons are tabulated in Table 12. The optimized hull shows 11% decrease in powering requirement. The *WJ* system efficiencies for the duct, and thrust deduction are improved by 6.7% and 1.32%, respectively. The jet efficiency shows a modest improvement of 0.1%.

Grid verification studies (Table 13) were conducted for the optimized geometry, using both barehull and self-propelled simulations. U_{I} is negligible and $U_{\mathrm{SN}} = U_{\mathrm{G}}$. For all cases, $0 < R < 1$, and monotonic convergence was achieved. $P < 2$ and reasonably close to 1. The U_{SN} values are similar to that obtained for the original geometry.

Previous optimization of the JHSS waterjet inlet curvature using the same methodology yielded a just 2% decrease in powering requirement. However, a drastic design modification by merging the adjacent inlets (Fig. 18) yielded an 8% decrease in powering requirement.

Table 12
Performance comparison

	Ori.	Opt.	Opt%Ori
	Resistance		
R_{BH}	4.32E+01	4.15E+01	−3.94
T_{NET}	5.21E+01	4.94E+01	−5.18
	Powering		
P_{E}	1.29E+02	1.24E+02	−3.94
P_{TE}	1.55E+02	1.47E+02	−5.18
P_{JSE}	1.80E+02	1.71E+02	−5.28
P_{PE}	2.04E+02	1.81E+02	−11.22
	Waterjet system efficiencies		
η_{duct}	8.82E−01	9.41E−01	+6.70
η_{jet}	8.63E−01	8.64E−01	+0.10
$(1-t)$	8.29E−01	8.40E−01	+1.32

Table 13
Optimized geometry verification

	S_3	S_2	S_1	R	P	U_{SN}
	BH with *CFD WJ* model					
R_{BH}	81.05	82.52	83.11	0.40	1.32	3.24
σ_{BH}	3.164	3.193	3.205	0.41	1.27	0.47
τ_{BH}	1.504	1.615	1.667	0.47	1.09	8.64
	SP with discretized duct					
Q_{SP}	1.832	1.861	1.874	0.45	1.16	2.36
T_{NET}	92.14	97.05	98.83	0.36	1.46	2.51
σ_{BH}	4.578	4.727	4.765	0.26	1.97	4.79
τ_{BH}	2.511	2.632	2.677	0.37	1.43	8.56
P_{PE}	171.68	178.84	181.12	0.32	1.65	7.22

7. Multi-objective optimization using *CFD WJ* model

The definition of the multi-objective optimization problem is based on the selection of three objective functions, that is, the total resistance at the speed of Fr = 0.3, 0.5 and 0.7. A subset of the previous base hulls has been adopted, in order to reduce the overall dimension of the design space and the complexity of the optimization problem accordingly. Since the objective functions are now three, the overall computational cost is triple, since three distinct runs of the HF solver are needed in order to produce the complete evaluation of one position in the design variable space.

For this multi-objective problem, the final solution of the problem is not represented by a single geometry, but by a suite of different solutions, representing the Pareto optimal set. In the case of three objective functions, the Pareto optimal set

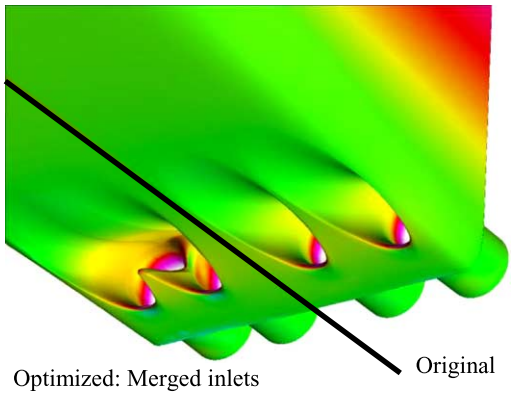

Fig. 18. Optimization of JHSS waterjet by merging the inlets. (Colors are visible in the online version of the article; http://dx.doi.org/10.3233/ISP-130098.)

is represented by a 3D surface, and its representation and visualization is not easy. Consequently, here are reported three different views, orthogonal to each coordinate axis related to an objective function. In each graph, the variety along the missing axis is lost, but we can observe to position of some interesting solutions and their performances in comparison with all the other solutions.

In Fig. 19, the three different views are reported. Red dot is indicating the best solution for function 1 (total resistance at $\mathrm{Fr} = 0.3$), green dot is indicating the best solution for function 2 (total resistance at $\mathrm{Fr} = 0.5$), and blue dot is indicating the best solution for function 3 (total resistance at $\mathrm{Fr} = 0.7$). It is evident how there is not improvement for the first objective function: this is probably connected to the fact that the base geometries are obtained with a particular emphasis to the central speed $\mathrm{Fr} = 0.5$. Looking at the second view, reporting second and third objective functions, a correlation is nearly evident, also if there are two distinct solutions representing the best for each objective function. On the contrary, the cloud of points in the space of the first and second objective function, as well as for the space of the first and third, is not crossing the vertical axis, showing a negative correlation. This means that an improvement on one of the objective if resulting into a deterioration of the other objective, that is, the two objectives are in opposition each other, and it is not possible to improve them together. A different parameterization scheme would be probably able to provide improved shapes also for the lower speed, while it is not possible to argue if the complete opposition between the objective functions is solvable by changing the parameterization or not.

In Fig. 20, a comparison between the section views for the original *DC* and one of the Pareto optimal solutions is reported, together with a comparison of the sectional area curve distributions. It is possible to clearly observe how there is a shift of the volume from inner to outer, and from stern to bow.

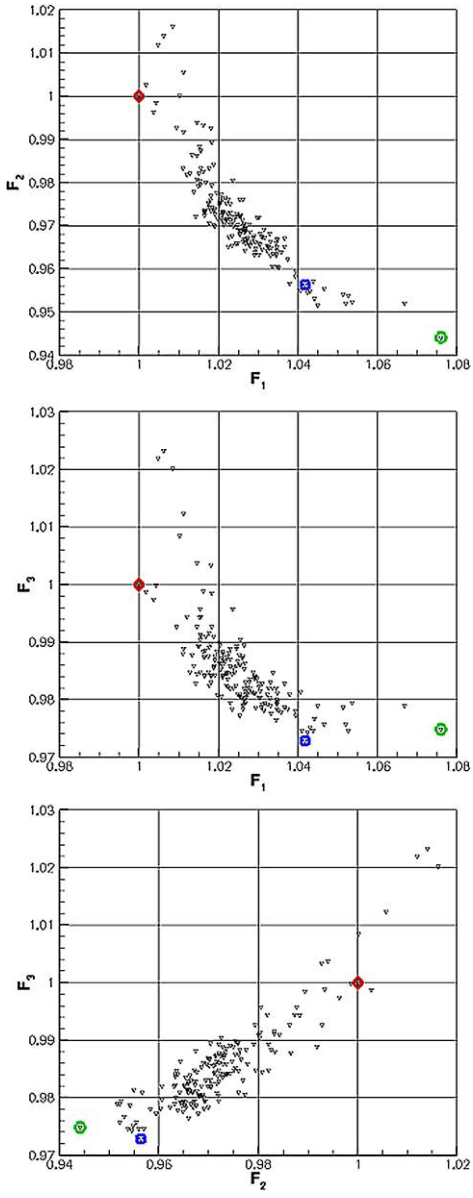

Fig. 19. Different views of the Pareto front for the multi-objective optimization problem. (Colors are visible in the online version of the article; http://dx.doi.org/10.3233/ISP-130098.)

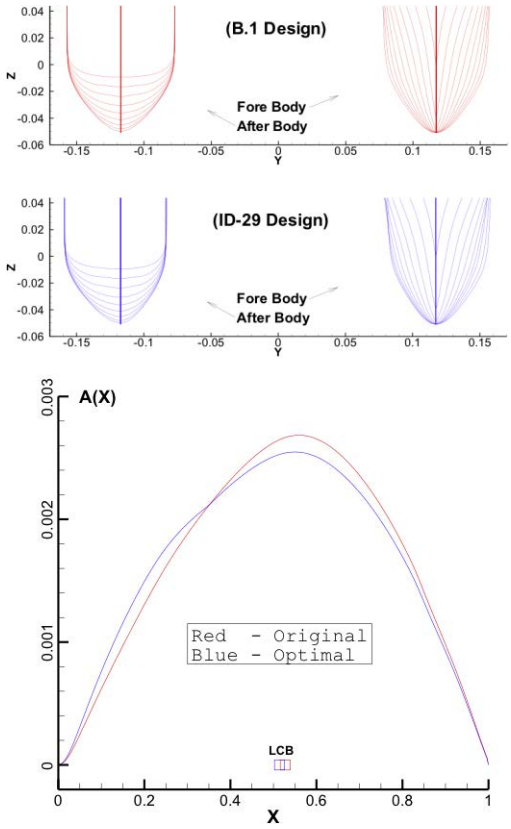

Fig. 20. Comparison between the original shape and the shape of best compromise solution for the three-objectives optimization problem. (Colors are visible in the online version of the article; http://dx.doi.org/10.3233/ISP-130098.)

8. Variable fidelity optimization for computational efficiency as proof of concept

The overall goal of the *VF/VP* approach is to obtain a significant *CPU* time reduction while at the same time, regain the same optimal solution as if we were solving the full-HF problem. Therefore, to assess the success of the *VF/VP* algorithm, the same optimization problem (same parameterization, constraints and objective function) for the *DC* has been carried out twice: first using the HF alone and then solving again the same problem using the *VF/VP* algorithm.

The parameterization scheme used is this test is the FFD approach. A single FFD box surrounds the hull: 4 parameters are used to shift the hull sections sideways, one is used to move the sections longitudinally and one is used to change the transom stern depth, for an overall number of 6 design variables.

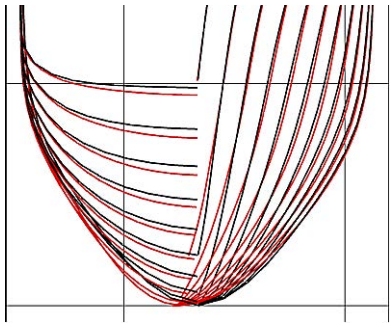

Fig. 21. Transversal sections of the original (black) and optimized hulls (red), both full HF and *VF/VP* solutions. (The colors are visible in the online version of the article; http://dx.doi.org/10.3233/ISP-130098.)

The shape of optimal design obtained by the HF and by *VF/VP* is substantially the same. The two geometries are superimposed in Fig. 21. In terms of computed objective function, the difference between full HF and *VF/VP* is of about 0.05% (6.4412 for the full HF, 6.4447 for the *VF/VP*). A great reduction is obtained instead in the computational cost: the HF optimization has required 940 HF evaluations of the objective function, while the *VF/VP* only needed 532 HF computations, plus 940 (almost inexpensive compared to HF SMD) LF evaluations. The overall *CPU* time reduction is therefore about 54%.

9. Conclusions

A simulation-based design optimization for the hull and *WJ* inlet was carried out for the powering optimization of *WJ* propelled *DC*, using integrated computational and experimental fluid dynamics. A *WJ* equipped *DC* was constructed and tested at two facilities with good agreement of data. The data was used to validate the LF and HF solvers and for the formulation of a simplified *CFD WJ* model that was used in conjunction with the LF optimization.

The particle swarm optimizer was used for single speed optimization at $\mathrm{Fr} = 0.5$, and genetic algorithms were used for multi speed optimization at $\mathrm{Fr} = 0.3$, 0.5 and 0.7. The multi-speed optimization showed design improvement at $\mathrm{Fr} = 0.5$ and 0.7, but not at $\mathrm{Fr} = 0.3$ since the design variables were obtained with a particular emphasis to the higher speeds. High fidelity simulation results for the optimized barehull geometry at $\mathrm{Fr} = 0.5$ indicated 4% reduction in resistance and the optimized *WJ* equipped geometry indicated 11% reduction in effective pump power required at self-propulsion.

Ongoing developments for geometric variability exploration, based on Karhunen–Loève expansion (*KLE*), have shown the capability of producing a wider range of design possibilities with deeper improvements [10,12]. Accordingly, a new optimization campaign [8] will be performed using reduced dimensional research spaces as

provided by *KLE* analysis. Meta-models and/or *VF/VP* approaches will be used to reduce the computational time.

Best design overall will be built and tested at INSEAN using the same experimental set-up as was used for the original model, to reduce the comparison errors. A complete set of tests is planned in the near future.

Future direction for design optimization is to include uncertainty effects on objectives and constraints. Ship designers have been always concerned with the uncertainties of the environment in which the ship sails (waves, winds, currents) since mostly not avoidable and often responsible for performance loss and failures. Robust and reliability-based design optimization methods, developed to improve product quality and reliability in industrial engineering, are to prevent performance drop when operating in off-design conditions and avoid dramatic failures in the case of exceptional events. The Bayesian approach is used to formulate the problems of robust design optimization (*RDO*) and reliability-based design optimization (*RBDO*). These require the uncertainty quantification (*UQ*) of the relevant simulation outputs over the stochastic inputs domain. The difficulty with exploiting this framework is mainly computational, since *UQ* requires the numerical integration of expensive simulation outputs over the uncertainties involved. Accordingly, research in *UQ* is an important precursory step for *RDO/RBDO* providing the impact of stochastic inputs on relevant outputs and identifying the most efficient *UQ* methods (such as meta-models based analyses) for the problem addressed. Earlier and current *UQ* research includes development and assessment of a framework for convergence, validation, and comparison with deterministic V&V of *UQ* studies. Applications include NACA 0012 hydrofoil with variable *Re* [22]; *UQ* of *DC* calm water resistance, sinkage and trim with variable Fr and geometry [10]; and *UQ* for *DC* resistance, motions and slamming loads in stochastic wave and variable geometry [12]. Future *RDO/RBDO* activities will focus on *DC* optimal design for reduced resistance, motions and slamming loads in stochastic wave at sea state 7 [11]. Geometric variability will be explored using *KLE* and, in order to keep the computational effort reasonable, optimization and *UQ* will be performed using metamodels and/or *VF/VP* methods.

Savings obtained are demonstrating the usefulness the *VF/VP* formulation. For this reason, further verification of the *VF/VP* approach will be also carried out in the near future, in order to gain more insight about the potential of this technique. Different formulations of the scheme, including the use of the variance estimation provided by the kriging meta-model in order to adapt the "trust region" radius dynamically will be explored.

Acknowledgements

The present research is supported by the Office of Naval Research, Grant N00014-08-1-0957, under the administration of Dr. Ki-Han Kim, and NICOP Grant N00014-01-543 under the administration of Dr. Patrick Purtell. The URANS computations were performed at the NAVY DoD Supercomputing Resource Center. The authors thank Thad Michael and Donnelly Martin of NSWCCD for their assistance.

References

[1] N.M. Alexandrova and R. Lewis, First-order approximation and model management in optimization, in: *Large-Scale PDE Constrained Optimization*, L.T. Biegler, O. Ghattas, M. Heinkenschloss and B. van Bloemen Waanders, eds, Lecture Notes in Computational Science and Engineering, Springer, Berlin/Heidelberg, 2003.

[2] P. Bassanini, U. Bulgarelli, E.F. Campana and F. Lalli, The wave resistance problem in a boundary integral formulation, *Surveys on Mathematics for Industry* **4** (1994), 151–194.

[3] N.W.H. Bulten, Numerical analysis of a *WJ* propulsion system, PhD thesis, University of Eindhoven, 2006.

[4] E.F. Campana, D. Peri, A. Pinto, Y. Tahara and F. Stern, Shape optimization in ship hydrodynamics using computational fluid dynamics, *Computer Methods in Applied Mechanics and Engineering* **196** (2006), 634–651.

[5] E.F. Campana, D. Peri, M. Kandasamy, Y. Tahara and F. Stern, Numerical optimization methods for ship hydrodynamic design, in: *SNAME Annual Meeting*, Providence, RI, USA, 2009.

[6] P.M. Carrica, R.V. Wilson, R.W. Noack and F. Stern, Ship motions using single-phase level set with dynamic overset grids, *Computer and Fluids* **36** (2007), 1415–1433.

[7] T. Castiglione, F. Stern, S. Bova and M. Kandasamy, Numerical investigation of the seakeeping behavior of a catamaran advancing in regular head waves, *Ocean Engineering* **38**(16) (2011), 1806–1822.

[8] X. Chen, M. Diez, M. Kandasamy, E.F. Campana and F. Stern, Optimization of waterjet propelled Delft-catamaran in calm water using Karhunen–Loève expansion and meta-heuristics, abstract submitted for presentation at *12th International Conference on Fast Sea Transportation, FAST 2013*, Amsterdam, The Netherlands, September 2013.

[9] K. Delaney, M. Donnely, M. Elbert and D. Fry, Use of RANS for waterjet analysis of a high-speed sealift concept vessel, in: *1st International Symposium on Marine Propulsors*, Trondheim, Norway, 2009.

[10] M. Diez, W. He, E.F. Campana and F. Stern, Uncertainty quantification of Delft catamaran resistance, sinkage and trim for variable Froude number and geometry using metamodels, quadrature and Karhunen–Loève expansion, *Journal of Marine Science and Technology* (2013), to appear.

[11] M. Diez, E.F. Campana and F. Stern, Reliability-based robust design optimization of Delft catamaran in stochastic wave, abstract submitted for presentation at *12th International Conference on Fast Sea Transportation, FAST 2013*, Amsterdam, The Netherlands, September 2013.

[12] W. He, M. Diez, E.F. Campana and F. Stern, URANS study of Delft catamaran total/added resistance, motions and slamming loads in head sea including irregular wave and uncertainty quantification for variable regular wave and geometry, *Ocean Engineering* (2013), to appear.

[13] ITTC Propulsion Committee, Testing and extrapolation methods, high speed marine vehicles, waterjets, propulsive performance prediction, ITTC-Recommended Procedures and Guidelines, 7.5-02-05-03.1, 2005.

[14] C. Janson and L. Larsson, A method for the optimization of ship hulls from a resistance point of view, in: *21st Symposium on Naval Hydrodynamics*, Norway, 1996.

[15] S. Jessup, M. Donnelly, D. Fry, D. Cusanelli and M. Wilson, Performance analysis of a four waterjet propulsion system for a large sealift ship, in: *27th Symposium on Naval Hydrodynamics*, Seoul, Korea, 2008.

[16] M. Kandasamy, S.K. Ooi, P. Carrica and F. Stern, Integral force/moment waterjet model for *CFD* simulations, *Journal of Fluid Engineering* **132**(10) (2010), 101103: 1–9.

[17] M. Kandasamy, S.K. Ooi, P. Carrica, F. Stern, E. Campana, D. Peri, P. Osborne, J. Cote, N. Macdonald and N.D. Waal, Multi-fidelity optimization of a high speed foil-assisted semi-planing catamaran for low wake, *Journal of Marine Science and Technology* **16**(2) (2011), 143–156.

[18] M. Kandasamy, W. He, T. Takai, Y. Tahara, D. Peri, E.F. Campana, W. Wilson and F. Stern, Optimization of *WJ* propelled high speed ships – JHSS and Delft catamaran, in: *Proceedings 11th International Conference on Fast Sea Transportation, FAST 2011*, Honolulu, HI, USA, 2011.
[19] E. Milanov, V. Chotukova and F. Stern, Experimental and simulation studies on fast Delft372 catamaran maneuvering and course stability in deep and shallow water, in: *Proceedings 11th International Conference on Fast Sea Transportation, FAST 2011*, Honolulu, HI, USA, 2011.
[20] E. Milanov, Model tests of waterjet propelled Delft 372 catamaran, BSHC Report KP092006/01, December 2010.
[21] M. Miozzi, Model tests of waterjet propelled Delft 372 catamaran, INSEAN-CNR internal report 2011-TR-011, 2011.
[22] S.M. Mousaviraad, W. He, M. Diez and F. Stern, Framework for convergence and validation of stochastic uncertainty quantification and relationship to deterministic verification and validation, *International Journal for Uncertainty Quantification* **3**(5) (2013), 371–395.
[23] D. Peri, Self-learning metamodels for optimization, *Ship Technology Research* **56** (2009), 94–108.
[24] D. Peri, E.F. Campana, Y. Tahara, T. Takai, M. Kandasamy and F. Stern, New developments in simulation-based design with application to high speed water-jet ship design, in: *28th Symposium on Naval Hydro-Dynamics*, Pasadena, CA, USA, 2010.
[25] F. Stern, A. Olivieri, J. Shao, J. Longo and T. Ratcliffe, Statistical approach for estimating intervals of certification or biases of facilities or measurement systems including uncertainties, *J. Fluids Eng.* **127** (2005), 604–610.
[26] F. Stern, P. Carrica, M. Kandasamy et al., Computational hydrodynamic tools for high-speed sealift, *Transactions SNAME* **114** (2006), 55–81.
[27] F. Stern, R. Wilson and J. Shao, Quantitative approach to V&V of *CFD* simulations and certification of *CFD* codes with examples, *International Journal Numerical Methods Fluids* **50**(11) (2006), 1335–1355, Special Issue: Advances in Computational Heat Transfer.
[28] F. Stern, P. Carrica, M. Kandasamy et al., Computational hydrodynamic tools for high speed sealift: Phase II final report, IIHR Technical Report No. 465, 2008.
[29] Y. Tahara, D. Peri, E.F. Campana and F. Stern, *CFD*-based multi-objective optimization of a surface combatant by using global optimization method, *Journal of Marine Science and Technology* **13** (2008), 95–116.
[30] Y. Tahara, T. Hino, M. Kandasamy, W. He and F. Stern, *CFD*-based multiobjective optimization of waterjet propelled high speed ships, in: *Proceedings 11th International Conference on Fast Sea Transportation, FAST 2011*, Honolulu, HI, USA, 2011.
[31] T. Takai, M. Kandasamy and F. Stern, Verification and validation study of URANS simulations for an axial *WJ* propelled large high-speed ship, *Journal of Marine Science and Technology* **16**(4) (2011), 434–447.
[32] T. Van Terwisga (Chairman), Report of the specialist committee on validation of waterjet test procedures, in: *Proceedings 24th International Towing Tank Conference II*, 2005, pp. 471–508.
[33] W. Wilson, D. Hendrix and J. Gorski, Hull form optimization for early stage ship design, *Naval Engineers Journal* **122**(2) (2010), 53–65.
[34] T. Xing and F. Stern, Factors of safety for Richardson extrapolation, *ASME J. Fluids Eng.* **132** (2010), 061403: 1–13.